Asociación Argentina
de Mecánica Computacional

Mecánica Computacional Vol XXV, pp. 1997-2018
Alberto Cardona, Norberto Nigro, Victorio Sonzogni, Mario Storti. (Eds.)
Santa Fe, Argentina, Noviembre 2006

# STRONG DISCONTINUITY APPROACH IN DYNAMIC FRACTURE SIMULATIONS

**A.E. Huespe[a], J. Oliver[b], P.J. Sanchez[a], S. Blanco[b], V.Sonzogni[a]**

[a]*CIMEC/INTEC – CONICET. Guemes 3450, 3000 - Santa Fe, Argentina,*
*http://www.cimec.unl.edu.ar*
[b]*E.T.S. d'Enginyers de Camins, Canals i Ports. Technical University of Catalonia (UPC)*
*Campus Nord UPC, Mòdul C-1, c/Jordi Girona 1-3, 08034 Barcelona, Spain*

**Keywords**: Dynamic fracture, cohesive models, embedded strong discontinuity.

**Abstract**. A cohesive model for simulating dynamic fracture problems is proposed. The use of an embedded strong discontinuity finite element recently introduced by Sancho *et al.* [9] in the context of quasi-static fracture problems is followed.

Two new ingredients of that model are added to extend the applicability of that formulation to dynamic fracture: a) the integration of the constitutive law by using the "implex" scheme determining a very robust procedure; b) the addition of a like-distributed damage law in a parallel direction to the principal crack allowing for the crack branching capture.

The formulation is particularly apt to capture the most important features of the dynamic crack propagation problem, such as the crack tip velocity and the crack branching phenomena. In the final sections of the paper, it is shown some numerical applications of this phenomenon.

## 1 INTRODUCTION

Dynamic fracture simulation, as a sub-area of computational failure mechanics, is becoming an increasingly area of research in last years. From the theoretical point of view, there are some aspects of dynamic fracture that are not well understood. Therefore, numerical simulation could help to determine, in some cases, how different variables take part in the evolution of the fundamental mechanisms involved in the phenomenon.

Perhaps, one of the most important aspects that should be explained in the near future is the correlation between the crack tip velocity and the crack branching process. Obviously, the crack branching arises due to an instability phenomenon inherent to the high velocity crack propagation process [1], but, at the present time, there is not a crack branching criterion capable of predicting its onset.

Cohesive models have been successfully applied to reach this objective. Some of the more important aspects of this phenomenon, which have been observed in experimental tests, could be acceptably captured by this approach. Several models using cohesive forces at the crack tip have been presented in the literature, not all of them based on finite elements, see for example Klein *et al.*[2].

Among the authors that firstly introduced cohesive forces in conjunction with interface finite elements, we can cite those of Needlemann *et al.* [3-4], Ortiz *et al.* [5], etc. More recently, Belytschko *et al.* have introduced the XFEM technology which, in conjunction with a cohesive model, could be satisfactorily applied to dynamic fracture [6].

In this work, we introduce a new model for the simulation of dynamic crack problems. It is based on an embedded strong discontinuity finite element approach, being that cohesive forces are introduced in the strong discontinuity interfaces. Therefore, the model can be understood to belong to the wider class of the cohesive models.

Section 2 describes the model and Section 3 presents the numerical applications. This section has been divided in two parts solving two kinds of problems. The first one is addressed to validate the model by means of the simulation of quasi-static crack propagation problems. On the other hand, the second set of numerical applications is addressed to the more specific problem of dynamic fracture simulation.

## 2 THE NUMERICAL MODEL: STRONG DISCONTINUITY APPROACH

### 2.1 Strong discontinuity kinematics

Let be given a body $\Omega$. An admissible displacement field in this body, $\mathbf{u}(\mathbf{x})$, exhibiting a strong discontinuity mode across a surface $S$ can be described by the following expression (see Figure 1):

$$\mathbf{u}(\mathbf{x}) = \bar{\mathbf{u}}(\mathbf{x}) + H_S(\mathbf{x})\,\boldsymbol{\beta}(\mathbf{x}) \quad ; \; H_S = \begin{cases} 1 \;\forall\; \mathbf{x} \in \Omega^+ \\ 0 \;\forall\; \mathbf{x} \in \Omega^- \end{cases} \tag{1}$$

where $\bar{\mathbf{u}}(\mathbf{x})$ denotes a smooth field, $H_S(\mathbf{x})$ is the Heaviside's step function shifted to $S$ which is multiplied by the displacement jump vector $\boldsymbol{\beta}(\mathbf{x})$ at the discontinuity interface $S$ whose normal is $\mathbf{n}$. This surface divides the body $\Omega$ in two disjoints parts, $\Omega^+$ and $\Omega^-$.

Following the papers of Simo *et al.* [7-8], it is more appropriate to impose the displacement and velocity boundary conditions when a slightly different format of (1) is introduced. Let the Heaviside's step function be replaced by the unit jump function $\mathsf{M}_S = \mathsf{H}_S - \varphi$, where

$\varphi$ is a continuous function being 0 in $\Omega^- \setminus S_k$, 1 in $\Omega^+ \setminus S_k$ and with a smooth transition across the region $S_k$ enclosing $S$ ($S_k \supset S$) (see [12] for more details). Then, the support of the function $\mathsf{M}_S$ is $S_k$. When this function is introduced for the kinematics enrichment, the admissible displacement, velocity and acceleration fields are described by:

$$\begin{aligned} \mathbf{u}(\mathbf{x}) &= \bar{\mathbf{u}}(\mathbf{x}) + \mathsf{M}_S(\mathbf{x})\,\boldsymbol{\beta}(\mathbf{x}) \quad ; \quad \mathsf{M}_S = \mathsf{H}_S - \varphi \\ \dot{\mathbf{u}}(\mathbf{x}) &= \dot{\bar{\mathbf{u}}}(\mathbf{x}) + \mathsf{M}_S(\mathbf{x})\dot{\boldsymbol{\beta}}(\mathbf{x}) \quad ; \\ \ddot{\mathbf{u}}(\mathbf{x}) &= \ddot{\bar{\mathbf{u}}}(\mathbf{x}) + \mathsf{M}_S(\mathbf{x})\,\ddot{\boldsymbol{\beta}}(\mathbf{x}) \quad ; \end{aligned} \tag{2}$$

and the strain field, being kinematically compatible with the discontinuous displacement field (2)-a, is:

$$\boldsymbol{\varepsilon}(\mathbf{x}) = \nabla^S \mathbf{u}(\mathbf{x}) = \underbrace{\bar{\boldsymbol{\varepsilon}}(\mathbf{x}) - (\nabla^S \varphi \otimes \boldsymbol{\beta})^{sym}}_{\text{regular (bounded)}} + \underbrace{\delta_S (\boldsymbol{\beta} \otimes \mathbf{n})^{\text{sym}}}_{\text{singular (unbounded)}} \quad ; \quad \bar{\boldsymbol{\varepsilon}}(\mathbf{x}) = \nabla^S \bar{\mathbf{u}} \tag{3}$$

The regular term in (3) determines the strain in the $\Omega \setminus S$ part of the body.

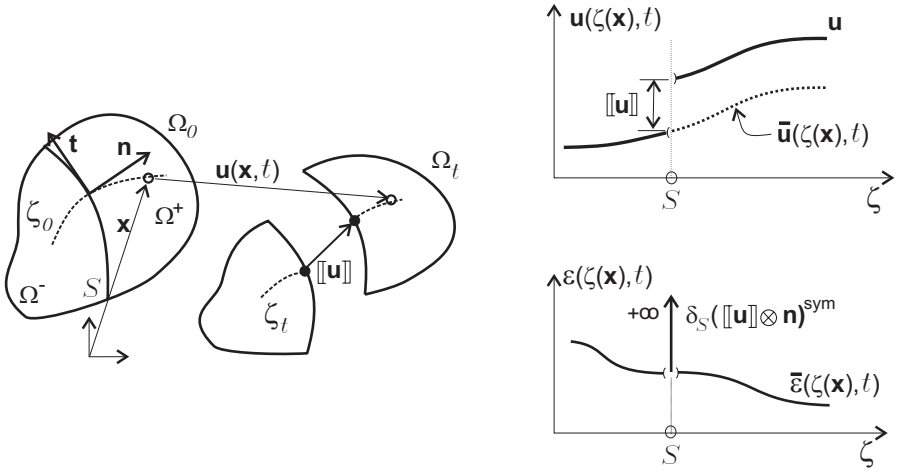


Figure 1: Strong discontinuity kinematics.

## 2.2 Problem governing equations

The classical strong format of the equations governing the strong discontinuity problem for a body like that shown in Figure 1, are the following:

$$\begin{array}{lll}
\rho\,\ddot{\mathbf{u}} = \nabla\cdot\boldsymbol{\sigma} + \rho_0\mathbf{b} & \forall(\mathbf{x},t)\in\Omega\setminus S\times[0,T] & \text{(momentum balance)} \quad (a) \\
\boldsymbol{\sigma}\cdot\boldsymbol{\nu} = \mathbf{t}^* & \forall(\mathbf{x},t)\in\Gamma_\sigma\times[0,T] & \text{(prescribed tractions)} \quad (b) \\
\left.\begin{array}{l}\mathbf{u}=\mathbf{u}^*\\ \dot{\mathbf{u}}=\dot{\mathbf{u}}^*\end{array}\right\} & \forall(\mathbf{x},t)\in\Gamma_u\times[0,T] & \text{(prescribed displacements and velocities)} \quad (c) \\
\left.\begin{array}{l}\mathbf{u}_o=\mathbf{u}^*(\mathbf{x},0)\\ \dot{\mathbf{u}}_o=\dot{\mathbf{u}}^*(\mathbf{x},0)\end{array}\right\} & \forall\mathbf{x}\in\Omega\setminus S\times[0] & \text{(prescribed } \textit{initial conditions}) \quad (d) \\
\boldsymbol{\sigma}^+\cdot\mathbf{n} = \boldsymbol{\sigma}^-\cdot\mathbf{n} & \forall(\mathbf{x},t)\in S\times[0,T] & \text{(outer traction continuity)} \quad (e) \\
\boldsymbol{\sigma}^+\cdot\mathbf{n} = \mathbf{t_c} & \forall(\mathbf{x},t)\in S\times[0,T] & \text{(equilibrium of cohesive forces)} \quad (f)
\end{array} \tag{4}$$

where the first equation represents the momentum balance equation in the domain $\Omega \setminus S$, being $\{\boldsymbol{\sigma}, \rho, \mathbf{b}\}$ the stress tensor, the material density and the mass force respectively. The following equations are the standard initial and boundary conditions. Tractions are prescribed on the contour $\Gamma_\sigma$, with normal vector $\boldsymbol{\nu}$ and displacement and velocities on $\Gamma_u$. Across the surface $S$ is prescribed the equilibrium of traction vectors. We assume that a cohesive force exist in $S$ given by the traction vector $\mathbf{t_c}$ (Eq. (4-f)), i.e. a discrete constitutive law (see section 2.5). Also we assume that an elastic model governs the response in $\Omega \setminus S$. Without loss of generality, it will be considered those problems where the mass forces are zero ($\mathbf{b} = \mathbf{0}$).

### 2.3 Weak formulation

Let us consider an admissible velocity space $V_0$ in $\mathbf{R}^2$ endowed with a jump:

$$V_0 = \left\{ \delta\dot{\mathbf{u}} \mid \delta\dot{\mathbf{u}} = \delta\dot{\overline{\mathbf{u}}} + M_S(\mathbf{x})\, \delta\dot{\boldsymbol{\beta}}(\mathbf{x}) \right\} \quad ; \quad \delta\dot{\overline{\mathbf{u}}} = \mathbf{0} \;\forall\, (\mathbf{x}, t) \in \Gamma_u \times [0, T] \tag{5}$$

where $\delta\dot{\overline{\mathbf{u}}}$ is a smooth field in $H_0^1$ and $\delta\boldsymbol{\beta} \in \mathbf{R}^2$. The governing equations (4) can be put in the variational format using the standard Virtual Power Principle:

$$\int \left( \rho\, \ddot{\mathbf{u}} \cdot \delta\dot{\mathbf{u}} + \boldsymbol{\sigma} : \nabla^{sym} \delta\dot{\mathbf{u}} \right) d\Omega - \int (\mathbf{t}^* \cdot \delta\dot{\mathbf{u}}) d\Gamma_\sigma = 0 \quad ; \quad \forall\, \delta\dot{\mathbf{u}} \in V_0 \tag{6}$$

that provides two sets of equations, that corresponds to the velocity variation given by the smooth part of (10) and the second comes from the jump variation $\delta\dot{\boldsymbol{\beta}}$:

$$\begin{aligned} &\int \left( \rho\, \ddot{\mathbf{u}} \cdot \delta\dot{\overline{\mathbf{u}}} + \boldsymbol{\sigma} : \nabla^{sym} \delta\dot{\overline{\mathbf{u}}} \right) d\Omega - \int (\mathbf{t}^* \cdot \delta\dot{\overline{\mathbf{u}}}) d\Gamma_\sigma = 0 \quad ; \quad \forall\, \delta\dot{\overline{\mathbf{u}}} \in H_0^1; \\ &\int \left( \rho\, \ddot{\mathbf{u}} \cdot M_S(\mathbf{x})\, \delta\dot{\boldsymbol{\beta}}(\mathbf{x}) + \boldsymbol{\sigma} : \nabla^{sym} (M_S(\mathbf{x})\, \delta\dot{\boldsymbol{\beta}}(\mathbf{x})) \right) d\Omega = 0 \quad ; \quad \forall\, \delta\dot{\boldsymbol{\beta}}. \end{aligned} \tag{7}$$

The second equation represents the weak balance of momentum in the region $S_k$ and is subjected to a particular treatment in the following discrete formulation.

### 2.4 Discrete weak approach: finite element with an embedded strong discontinuity

Let a linear triangular finite element (CST) be given. The linear kinematics of this element is enriched by adding a strong discontinuity mode following the ideas proposed in the approach given by equations (2). The interpolations for displacement, velocity and acceleration fields are given by :

$$\begin{aligned} &\mathbf{u}^h(\mathbf{x}) = N_i(\mathbf{x})\, \overline{\mathbf{u}}_i + \mathsf{M}_S^e(\mathbf{x}) \boldsymbol{\beta}^e \quad ; \qquad \mathsf{M}_S^e(\mathbf{x}) = (\mathsf{H}_S - N^+) \\ &\dot{\mathbf{u}}^h(\mathbf{x}) = N_i(\mathbf{x})\, \dot{\overline{\mathbf{u}}}_i + \mathsf{M}_S^e(\mathbf{x}) \dot{\boldsymbol{\beta}}^e \quad ; \qquad e = 1,2,\ldots, n_{act} \\ &\ddot{\mathbf{u}}^h(\mathbf{x}) = N_i(\mathbf{x})\, \ddot{\overline{\mathbf{u}}}_i + \mathsf{M}_S^e(\mathbf{x}) \ddot{\boldsymbol{\beta}}^e \; ; \end{aligned} \tag{8}$$

where $N_i$ are the standard shape functions of the CST element and $\{\overline{\mathbf{u}}_i, \dot{\overline{\mathbf{u}}}_i, \ddot{\overline{\mathbf{u}}}_i\}$ correspond to the interpolation parameters representing the displacements, the velocities and the accelera-

tions of node $i$. The kinematics enrichment, given by the discrete unit jump function $\mathsf{M}_{\mathrm{S}}^{\mathrm{e}}(\mathbf{x})$ times the jump $\boldsymbol{\beta}^e \in \mathbf{R}^2$, have a support of one element and is built by subtracting to the Heavise's function one of the shape functions $N^+$, which, and following to Sancho *et al.* [9], is selected such that it verifies the condition, see Figure 2:

$$N^+ = \arg\left( \max_{i=1,2,3} \left[ \frac{|\nabla N_i \cdot \mathbf{n}|}{\|\nabla N_i\|} \right] \right); \tag{9}$$

being $\mathbf{n}$ the normal vector to the discontinuity surface $S$. The enrichment terms in (8) are added only in those elements that have previously reached the bifurcation condition, or the criterion to activate the discontinuity $\boldsymbol{\beta}$. There are a variable number $n_{act}$ of finite elements in that condition, as the time evolves along the numerical simulation.

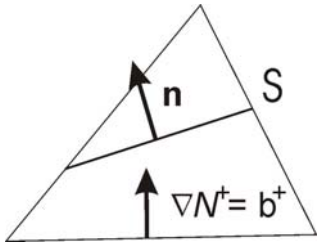


Figure 2 : Strong discontinuity kinematics.

The strain being compatible with (8) is then given by:

$$\boldsymbol{\varepsilon}^h(\mathbf{x}) = \nabla^S \mathbf{u}^h(\mathbf{x}) = \overbrace{\nabla^s \bar{\mathbf{u}}^h(\mathbf{x})}^{\bar{\boldsymbol{\varepsilon}}(\mathbf{x})} - (\mathbf{b}^+ \otimes \boldsymbol{\beta})^{sym} \quad ; \quad \forall\, \mathbf{x} \in \Omega \setminus S \,; \tag{10}$$

where $\mathbf{b}^+ = \nabla N^+$ .

The virtual power expression (6) is approached by using the discrete space (8), and the following admissible velocity space:

$$V_0^h = \left\{ \delta \dot{\mathbf{u}}^h \mid \delta \mathbf{u}^h = N_i \delta \bar{\mathbf{u}}_i + \mathsf{M}_{\mathrm{S}}^{\mathrm{e}}(\mathbf{x})\, \delta \dot{\boldsymbol{\beta}}^e(\mathbf{x}) \right\} \quad . \tag{11}$$

Then, the equation corresponding to the variation of the parameter $\delta \bar{\mathbf{u}}_i$, the discrete counterpart of equation (7)-a, yields:

$$\delta \bar{\mathbf{u}}_i \cdot \left[ \int \left( \rho\, N_i N_j \ddot{\mathbf{u}}_j + \boldsymbol{\sigma}_{ij} : \nabla^{sym} N_i \right) d\Omega - \int (N_i \mathbf{t}^*) d\Gamma_\sigma \right] = 0 \quad ; \forall \delta \bar{\mathbf{u}}_i, \quad i = 1,\ldots, N_{nods} \,. \tag{12}$$

On the other hand, the discrete counterpart of the second equation (7)-b is subjected to a different treatment. We assume that the width of the region $S_k$, which agrees with the size of the finite elements, goes to zero as the mesh is refined. Therefore, the term corresponding to the inertial forces in (7)-b will be neglected. The remaining part of that equation represents the weak equilibrium condition of the traction vector across the discontinuity $S$.
Instead of using a weak condition to impose the equilibrium condition, we will be evaluating it by means of a point-wise strong format:

$$\mathbf{t}_{\mathbf{c}}^e - \boldsymbol{\sigma}^e \cdot \mathbf{n}^e = \mathbf{0} \qquad ; \qquad \forall e \in \{1,2,\ldots, n_{act}\} \,. \tag{13}$$

There is one vectorial equation (13) for every element $e$ having an active discontinuous mode. The term $\mathbf{t}_\mathbf{c}^e$ is the cohesive force in the discontinuity $S$ and $\boldsymbol{\sigma}^e$ is the stress tensor in the regular part of the finite element $e$ (in $\Omega^e \setminus S$). We recall that, being a CST finite element, there is a constant stress tensor $\boldsymbol{\sigma}^e$ in $\Omega^e \setminus S$.

The criterion that defines the inception of the discontinuous mode into the finite element is based on the maximum principal stress component $\sigma_I$. The crack begins to open whenever $\sigma_I > \sigma_u$, with $\sigma_u$ being the material tensile strength, and propagates orthogonally to the principal stress direction.

### 2.5 Cohesive model and traction vector continuity in S

Following the work of Sancho *et al.* [9], we define a cohesive central force model as representative of the cohesive forces acting in the discontinuity $S$. In that case, the traction vector $\mathbf{t}_\mathbf{c}$, at time $t$, is defined to be collinear with the displacement jump $\boldsymbol{\beta}$ and given by the law:

$$\begin{aligned} \mathbf{t}_\mathbf{c} &= f(\tilde{\beta})\frac{\boldsymbol{\beta}}{\tilde{\beta}} \quad ; \quad f(\tilde{\beta}) = \sigma_u \exp(-\frac{\sigma_u \tilde{\beta}}{G_f}) \; ; \\ \tilde{\beta} &= \max_\tau(\|\boldsymbol{\beta}\|) \quad ; \quad \forall 0 \le \tau \le t \; ; \end{aligned} \tag{14}$$

where $G_f$ is the material parameter representing the fracture energy. Forcing an elastic unloading process in the outside part of $S$ (in $\Omega \setminus S$), and establishing the point-wise strong equilibrium condition (13) between the elastic stress $\boldsymbol{\sigma}_{\Omega\setminus S}$ and $\mathbf{t}_\mathbf{c}$, it results the equilibrium equation:

$$\mathbf{t}_\mathbf{c} = f(\tilde{\beta})\frac{\boldsymbol{\beta}}{\tilde{\beta}} = \quad \mathbf{n}\cdot\mathbf{C}^e : (\bar{\boldsymbol{\varepsilon}} - (\mathbf{b}^+ \otimes \boldsymbol{\beta})^{sym}) = \boldsymbol{\sigma}_{\Omega\setminus S}\cdot\mathbf{n} \; ; \tag{15}$$

being $\mathbf{C}^e$ the Hooke elastic tensor, and therefore:

$$\left(\frac{f(\tilde{\beta})}{\tilde{\beta}}\mathbf{1} + \mathbf{n}\cdot\mathbf{C}^e\cdot\mathbf{b}^+\right)\cdot\boldsymbol{\beta} = \mathbf{n}\cdot\mathbf{C}^e : \bar{\boldsymbol{\varepsilon}} \; ; \tag{16}$$

which determines the jump $\boldsymbol{\beta}$ as a function of $\bar{\boldsymbol{\varepsilon}}$.

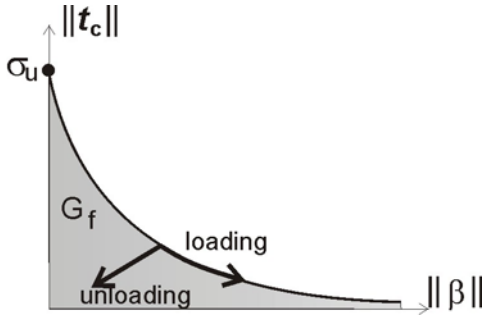


*Figure 3: Cohesive model*

The assumption that the material should be constrained to follow an elastic unloading process outside the discontinuity $S$, independently of the strain values in all of their components, could introduce a severe stress locking phenomenon. This effect that was widely studied in the past, have been observed to be provoked by a deficient finite element approach, *i.e.* an inadequate kinematics, and therefore, an incorrect numerical approach. The correct selection of a finite element kinematics, therefore, is a topic in this field.

But things are harder in dynamic crack propagation problems. There, a crack branching process is to be expected in most of the problems when a high crack front velocity is reached. In those cases, three cracks will intersect one finite element in the position where the branching condition is verified. So, if the same type of discrete approach for the strong discontinuity finite element is held, what means only one embedded crack mode by FE, the kinematics will not be able to capture the strain mode required by the phenomenon, and a severe stress locking problem will happen. The stresses will be unrealistically high, mainly in that component orthogonal to $\mathbf{n}$, perturbing the crack propagation phenomena inducing the crack arrest of one of the branches.

To remove this deficient behavior, we introduce a material response, in $\Omega \setminus S$, that limits the value of the stress component $\sigma_{mm}$, where $\mathbf{m}$ is the orthogonal direction to $\mathbf{n}$. The response of this component, as a function of the strain in $\Omega \setminus S$, can be understood as given by a non-isotropic continuum damage model which is described as follows:

$$
\begin{aligned}
& t_{mm}(\tilde{\gamma}) = \sigma_u \exp(-\frac{\sigma_u \tilde{\gamma}}{G_{fm}}) \frac{S}{\tilde{S}} ; \\
& S = \mathbf{m} \cdot \left( \mathbf{C}^e : (\bar{\boldsymbol{\varepsilon}} - (\mathbf{b}^+ \otimes \boldsymbol{\beta})^s) \right) \cdot \mathbf{m} ; \\
& \tilde{S} = \max_{\tau} \left| S(\mathbf{x}, t) \right| \quad ; \quad \forall\, 0 \le \tau \le t ; \\
& \tilde{\gamma} = \frac{S - \sigma_u}{E} ;
\end{aligned}
\tag{17}
$$

and is motivated by the origin of a new distributed cracking pattern, orthogonal to the main crack direction opening in mode I, and whose cohesive law, a central force model, is governed by a similar form to (14), with a regularized fracture energy defined by: $G_{fm} = G_f / h^e$, where $h^e$ is a representative size of the finite element.

The stress tensor $\boldsymbol{\sigma}$ is computed by knowing the traction vector in the direction $\mathbf{n}$, that based on Equation (14) is the vector $\mathbf{t_c}$, and the component $t_{mm}$ as follows, see Figure 4:

$$
\boldsymbol{\sigma} = (\mathbf{t_c} \cdot \mathbf{n})(\mathbf{n} \otimes \mathbf{n}) + (\mathbf{t_c} \cdot \mathbf{m})[(\mathbf{n} \otimes \mathbf{m}) + (\mathbf{m} \otimes \mathbf{n})] + t_{mm}(\mathbf{m} \otimes \mathbf{m}). \tag{18}
$$

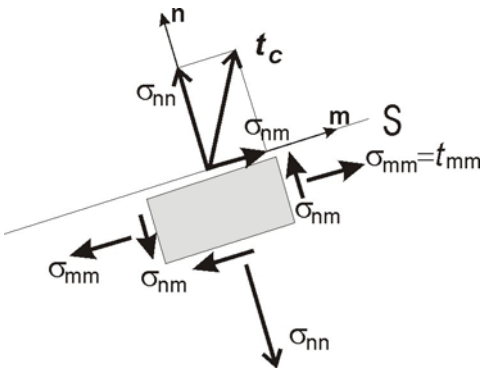


Figure 4: Stress tensor $\boldsymbol{\sigma}\left(\bar{\boldsymbol{\varepsilon}}\right)$

### 2.6 Time integration scheme

After using equation (13) to compute the parameters $\boldsymbol{\beta}$, the remaining discrete equation (12) can be written in a standard matrix format as:

$$\mathbf{M}[\ddot{\bar{\mathbf{u}}}] + \mathbf{K}[\bar{\mathbf{u}}] = \mathbf{F}_{ext}\,; \tag{19}$$

where $\mathbf{M}$ and $\mathbf{K}$ represent the global mass and stiffness matrices; $[\bar{\mathbf{u}}]$ and $\mathbf{F}_{ext}$ are the vector of displacements and external loads. It should be observed that, in the present procedure, the vector $[\bar{\mathbf{u}}]$ does not include the $\boldsymbol{\beta}$ parameters, and therefore, the system of equations (19) is identical to that provided by the CST element in dynamical problems without including strong discontinuity modes, that is, the mass and stiffness matrices are exactly the same. Therefore, from the computational point of view, the present implementation is very advantageous respect to alternative strong discontinuity formulations.

#### 2.6.1 Implicit-explicit integration scheme for the constitutive model

The time integration of (19) is also a standard issue. Proposing a classical implicit Newmark procedure for the time step $r+1$, displacement and velocities are approached by

$$\begin{aligned} \mathbf{u}^{r+1} &= \mathbf{u}^{r} + \Delta t\, \dot{\mathbf{u}}^{r} + \Delta t^2\, [(0.5-\beta)\ddot{\mathbf{u}}^{r} + \beta \ddot{\mathbf{u}}^{r+1}] \quad ; \\ \dot{\mathbf{u}}^{r+1} &= \dot{\mathbf{u}}^{r} + \Delta t\, [(1-\gamma)\ddot{\mathbf{u}}^{r} + \gamma \ddot{\mathbf{u}}^{r+1}] \quad ; \end{aligned} \tag{20}$$

where the time increment $\Delta t$ is the interval time between $t^{r+1}$ and $t^{r}$, $\beta$ and $\gamma$ are two real parameters that we have set to 0.25 and 0.5 respectively for all numerical applications in the next section, recovering a non-dissipative 2nd. order accurate scheme.

Inserting (20) into (19) and working out the equations, the final problem result a set of nonlinear equations in $\mathbf{u}^{r+1}$, where the stresses $\boldsymbol{\sigma}^{r+1}$ should be determined as a function of that displacement.

It should be considered that different alternatives or schemes can be used to define the stresses $\boldsymbol{\sigma}^{r+1}$ as a function of $\mathbf{u}^{r+1}$. And therefore, depending on it, some algorithmic properties, such as numerical stability and robustness, will change.

Following the stress integration procedure presented in Oliver *et. al.* [10] that was called

"implex" (implicit/explicit) scheme, we compute $\boldsymbol{\sigma}^{r+1}$ by using the following algorithm. Let be given $\mathbf{u}^{r+1}$, and therefore $\bar{\boldsymbol{\varepsilon}}^{r+1} = \nabla^{sym}\mathbf{u}^{r+1}$, then stress computing is performed as follows:

***Box 1: Explicit stage in the "implex" stress update algorithm.***

a) Solve $\boldsymbol{\beta}^{r+1}$ from:

$$f(\tilde{\beta}^r)\frac{\boldsymbol{\beta}^{r+1}}{\tilde{\beta}^r} = \mathbf{n}\cdot\mathbf{C}^e : (\bar{\boldsymbol{\varepsilon}}^{r+1} - (\mathbf{b}^+ \otimes \boldsymbol{\beta}^{r+1})^{sym});$$

b) determine $\mathbf{t}_\mathbf{c}^{r+1}$ from

$$\mathbf{t}_\mathbf{c}^{r+1} = f(\tilde{\beta}^r)\frac{\boldsymbol{\beta}^{r+1}}{\tilde{\beta}^r};$$

c) determine $t_{mm}^{r+1}$ from:

$$t_{mm}^{r+1}(\tilde{\gamma}^r) = \sigma_u \exp(-\frac{\sigma_u \tilde{\gamma}^r}{G_{fm}})\frac{S^{r+1}}{\tilde{S}^r};$$

$$S^{r+1} = \mathbf{m}\cdot\left(\mathbf{C}^e : (\bar{\boldsymbol{\varepsilon}}^{r+1} - (\mathbf{b}^+ \otimes \boldsymbol{\beta}^r)^{sym})\right)\cdot\mathbf{m};$$

d) evaluate the stress $\boldsymbol{\sigma}^{r+1}$ by means of:

$$\boldsymbol{\sigma}^{r+1} = (\mathbf{t}_\mathbf{c}^{r+1}\cdot\mathbf{n})(\mathbf{n}\otimes\mathbf{n}) + (\mathbf{t}_\mathbf{c}^{r+1}\cdot\mathbf{m})[(\mathbf{n}\otimes\mathbf{m}) + (\mathbf{m}\otimes\mathbf{n})] + t_{mm}^{r+1}(\mathbf{m}\otimes\mathbf{m}); \qquad (21)$$

where the terms representing the internal variables of the model, $\tilde{\beta}$ and $\tilde{\gamma}$, are fixed to be that values obtained at previous step $r$ by means of an implicit integration of equations (16) and (17). In this way, we are performing two stress integrations per time step.

The stress $\boldsymbol{\sigma}^{r+1}$, from (21), is used to compute the momentum balance equation at step $r+1$. Therefore, the effective algorithmic tangent tensor $\boldsymbol{A}^{tg}$ to be used in the Newton-Raphson procedure corresponds to the derivative of Equation (21) of Box 1: $\boldsymbol{A}^{tg} \overset{def}{=} \partial_{\bar{\boldsymbol{\varepsilon}}^{r+1}}\boldsymbol{\sigma}^{r+1}$.

Oliver *et al.* [10] have studied the necessary conditions by which an implicit/explicit procedure yields a well behaved algorithmic procedure. Following a similar analysis, it is possible to conclude that the condition $\det(\mathbf{n}\cdot\mathbf{C}^e\cdot\mathbf{b}^+) > 0$, in the present approach, is necessary to reach good numerical properties. It is straightforward to shown that, if this condition is verified, the matrix on the left hand side part in Equation (16) would be non-singular, taking into account that $f(\tilde{\beta})/\tilde{\beta}$ is a positive monotonous decreasing function in time, and therefore the jump $\boldsymbol{\beta}$ would exist and be uniquely determined for all $\bar{\boldsymbol{\varepsilon}}$. Furthermore, it was shown in reference [10] that selecting a symmetric finite element, the above mentioned condition would change to: $\det(\mathbf{b}^+\cdot\mathbf{C}^e\cdot\mathbf{b}^+) > 0$, which is trivially verified. The proposed technique of selecting the vector $\mathbf{b}^+$ by means of procedure (9), in the paper of Sancho *et al.* [9], partially mitigates the restriction imposed by the condition of non-singular matrix $[\mathbf{n}\cdot\mathbf{C}^e\cdot\mathbf{b}^+]$. But it is not enough. In fact, it is possible to observe negative values of $\det(\mathbf{n}\cdot\mathbf{C}^e\cdot\mathbf{b}^+)$ for distorted

meshes, what induces the failure of the numerical scheme. We propose to substitute the vector $\mathbf{n}$, in equation (15), by a unit vector $\hat{\mathbf{n}}$ resulting from the convex combination of $\mathbf{n}$ and $\mathbf{b}^+$:

$$\hat{\mathbf{n}} = \frac{\theta \mathbf{n} + (1-\theta)\mathbf{b}^+}{\left\| \theta \mathbf{n} + (1-\theta)\mathbf{b}^+ \right\|} . \tag{22}$$

The parameter $\theta$ is obtained by the condition that $\theta < \theta_c$, where:

$$g(\theta_c) = \det\left[ (\theta_c \, \mathbf{n} + (1-\theta_c)\mathbf{b}^+) \cdot \mathbf{C}^e \cdot \mathbf{b}^+ \right] = 0 . \tag{23}$$

It must be observed that, in those cases where $\det(\mathbf{n} \cdot \mathbf{C}^e \cdot \mathbf{b}^+) < 0$, there exist, and it is unique, a parameter $\theta_c \in (0,1)$ verifying (23). In fact, and assuming plane stress or plane strain condition, the function $g$ is a second degree equation in $\theta_c$, with $g(0) < 0$ and $g(1) > 0$. The vector $\hat{\mathbf{n}}$ should be determined only one time per activated finite element in the complete simulation. Therefore, the computational cost of evaluating (23) is negligible.

With the mentioned modification, the present scheme restores two interesting property presented in the original proposal of Oliver *et al.* [10]:

- it provides an algorithmic tangent tensor $\boldsymbol{A}^{tg}$ which is non-singular, yielding a well-posed set of equations;
- the algorithmic tangent tensor $\boldsymbol{A}^{tg}$ does not depend on $\bar{\boldsymbol{\varepsilon}}$. So, the implict/explicit stress $\boldsymbol{\sigma}$ is linear with $\bar{\boldsymbol{\varepsilon}}$, what means that only one iteration per step is necessary to get convergence, whatever be the required tolerance.

## 3 NUMERICAL APPLICATIONS

In the first part of this section, we validate the finite element model by using a set of typical benchmark tests corresponding to quasi-static fracture propagation problems. All of them are well known tests in fracture mechanics. After being validated the model, we show, in a second part, a series of numerical simulations corresponding to dynamical crack propagation problems.

There is a point related to the numerical implementation which should be remarked. Following to Sancho *et al.* [9], we allow the normal vector $\mathbf{n}$ to change slightly its direction after the beginning of the strong discontinuity regime. This rotation is allowed while the crack opening is less than a fraction of the value $\beta^{crit} = G_f / \sigma_u$, see details in [9], and it becomes a very important aspect to get good numerical results. Nevertheless, the introduction of the distributed damage (17) in the parallel direction of the crack, alleviates this *ad-hoc* requirement, in the sense that a much lower fraction of $\beta^{crit}$ (in the following quasi-static problems it was less than 1%) is needed to reach an acceptable result.

### 3.1 Quasi-static crack propagation problems

In the three following examples, we present the numerical results obtained with several meshes, in order to show the convergence behavior of the numerical solution with the mesh. The finite element sizes used in the analysis have been $h^e(Mesh\,1)$, $0.5h^e(Mesh\,2)$ and $0.25h^e(Mesh\,3)$ respectively.

### 3.1.1 DCB test with diagonal compressive loads

This test has been reported originally by Rots [11] and later by [12]. It corresponds to the classical DCB test in plane stress state, see Figure 5-a. Initially the specimen is subjected to an incrementally compressive diagonal loads $F_2$ jointly with a opening ones $F_1$ applied on the inner faces of the notch. In a second stage, the level of the compressive loads is held constant while the opening ones grow linearly (see Figure 5-b).

The experimental test shows a crack, propagating from the notch root toward the specimen top and displaying an angle of $\alpha = 71^o$ with the horizontal.

The material parameters are: Young's modulus $E = 30500\,[MPa]$, Poisson's ratio: $\nu = 0.2$, fracture energy: $G_f = 0.1\,[N/m]$, tensile strength: $\sigma_u = 3.0\,[MPa]$ and specimen thickness: $50.8\,mm$.

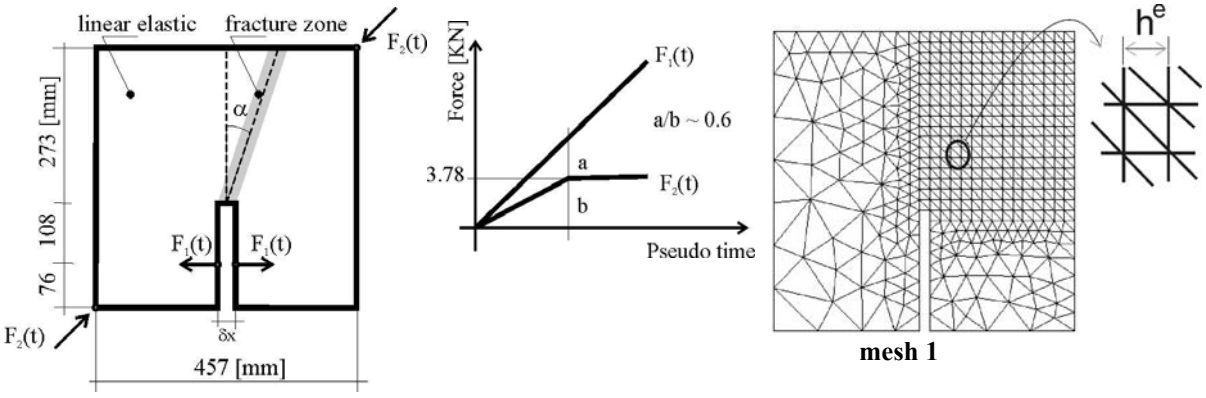


Figure 5: DCB test. (a) geometrical and loading model, (b) FE mesh.

We use three meshes with the pattern shown in Figure 5-b. It must be observed that it has been intentionally designed to provide a very challenging test for the proper capturing of the crack path across the mesh. All three meshes have identical geometry in the notch root.

We have controlled the numerical process by using a displacement control method. It has been fixed the incremental displacement **δx** per step in the inner faces of the notch (called Crack Mouth Opening Displacement CMOD) in those nodes where the horizontal forces $F_1$ are applied. Numerical and experimental results of the structural response load $F_1$ *vs.* CMOD are displayed in Figure 6. The discontinuity path is shown in Figure 7.

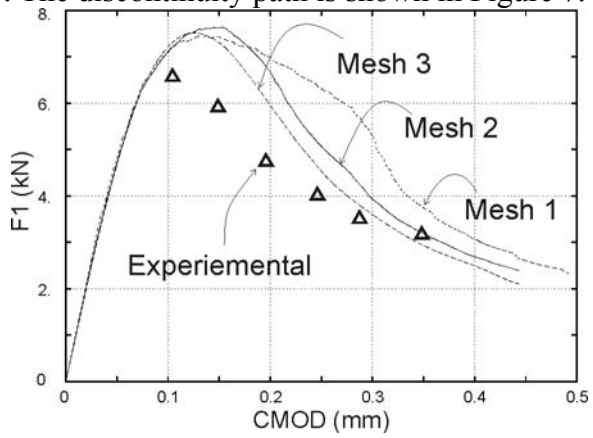


Figure 6: DCB test. Load *vs.* CMOD curves obtained with three meshes. Comparison with experimental results.

Rotations of the crack direction at each finite element have been allowed until it was reached a crack opening value. This value has been, respectively, 0.01, 0.005 and 0.003 times $\beta^{crit}$ for the meshes 1, 2 and 3.

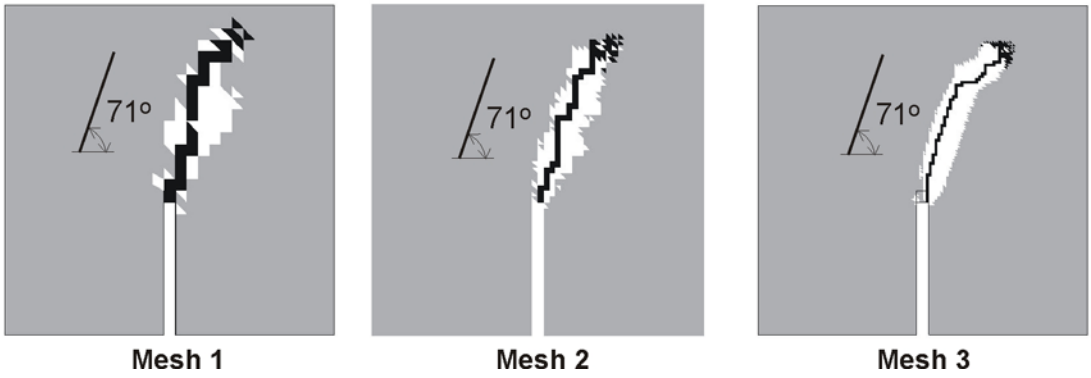


Figure 7: DCB test. Crack paths for different meshes and procedures

### 3.1.2 A notched beam bending test

The second test corresponds to a bending test of a notched beam with a thickness equal to 100*mm*, as is displayed in Figure 8-a. The analysis was carried out in plane stress conditions and it was imposed a vertical displacement $\Delta \mathbf{u}_y$ control in the node where the vertical downward load $P$ was applied. The two meshes of Figure 8-b were used.

Figure 9 displays the loads *vs.* vertical displacement curves while Figure 10 shows the crack path solutions obtained in the two cases. These results agree with the experimental ones.

The two solutions have been obtained by allowing the rotation of the discontinuity normal vector $\mathbf{n}$ until the crack opening reach the value 0.01 and 0.005 times $\beta^{crit}$ for meshes 1 and 2 respectively.

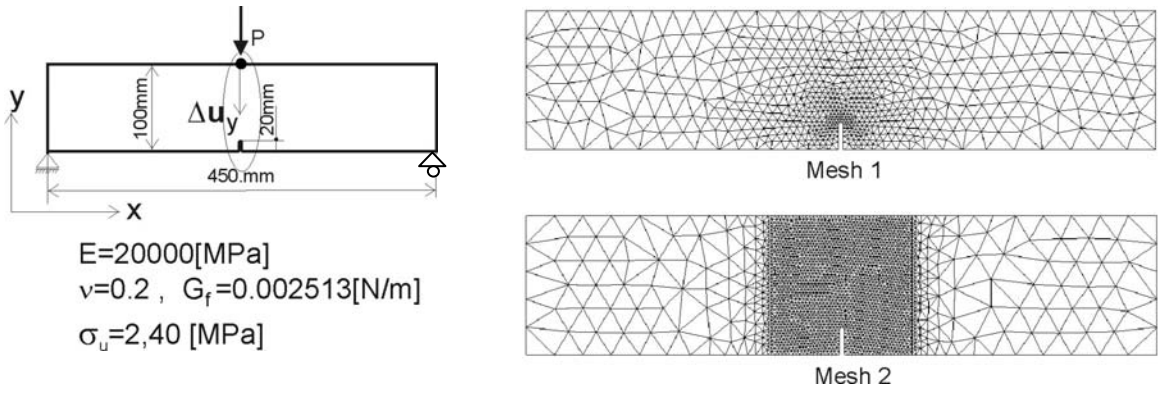


Figure 8: Beam bending test. (a) Geometrical and material properties. (b) Finite element discretizations.

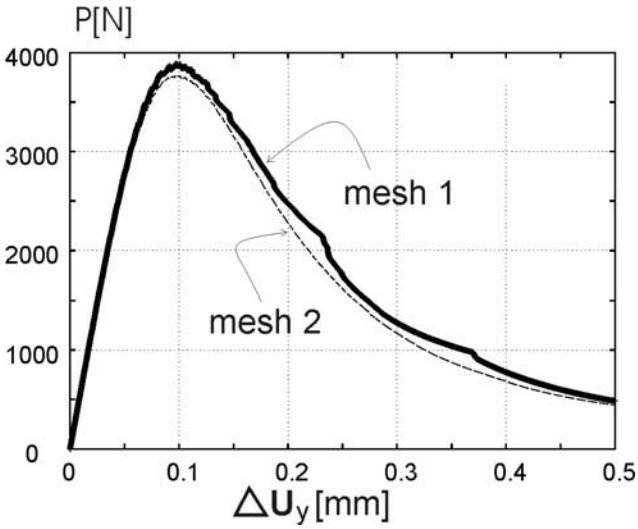


Figure 9: Beam bending test. Load *vs* Displacement curves

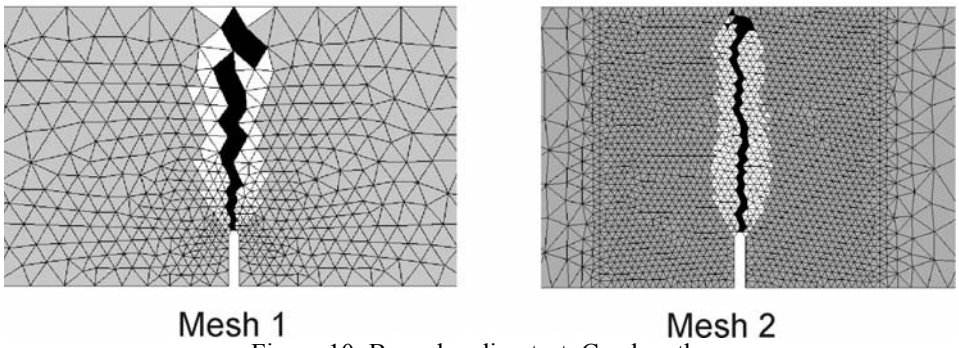


Figure 10: Beam bending test. Crack paths

### 3.1.3 Four point beam bending test

The last quasi-static test is a notched four point bending problem reported in [12], see Figure 11-a for the geometry and the material parameters. The analysis was held with plane stress conditions by controlling the Crack Mouth Sliding Displacement (CMSD). It was imposed CMSD values proportional to $\Delta u = 8E\text{-}04[mm]$.

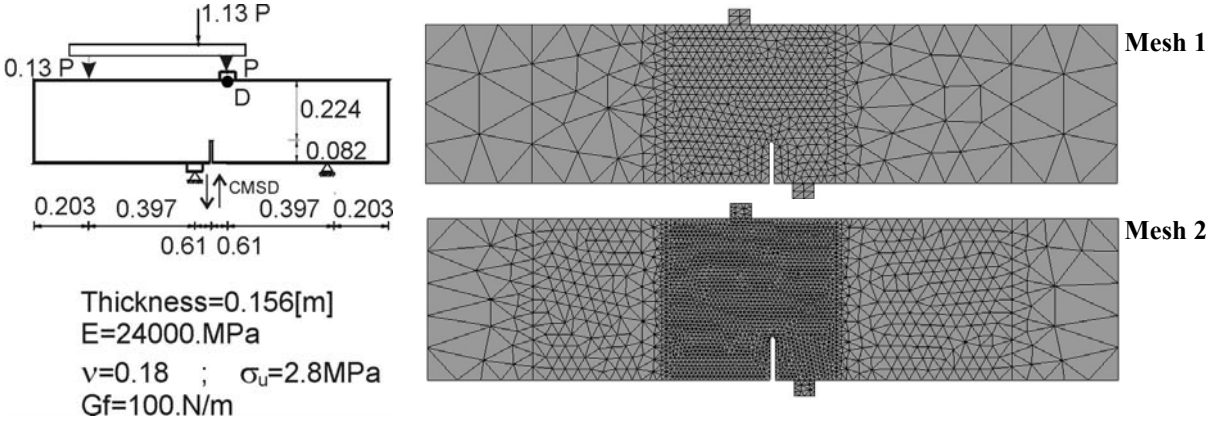


Figure 11: Four point beam bending test. (a) Geometrical and material description. (b) Finite element discretizations.

Figure 12 shows the results that have been obtained with both meshes and the different time step lengths.

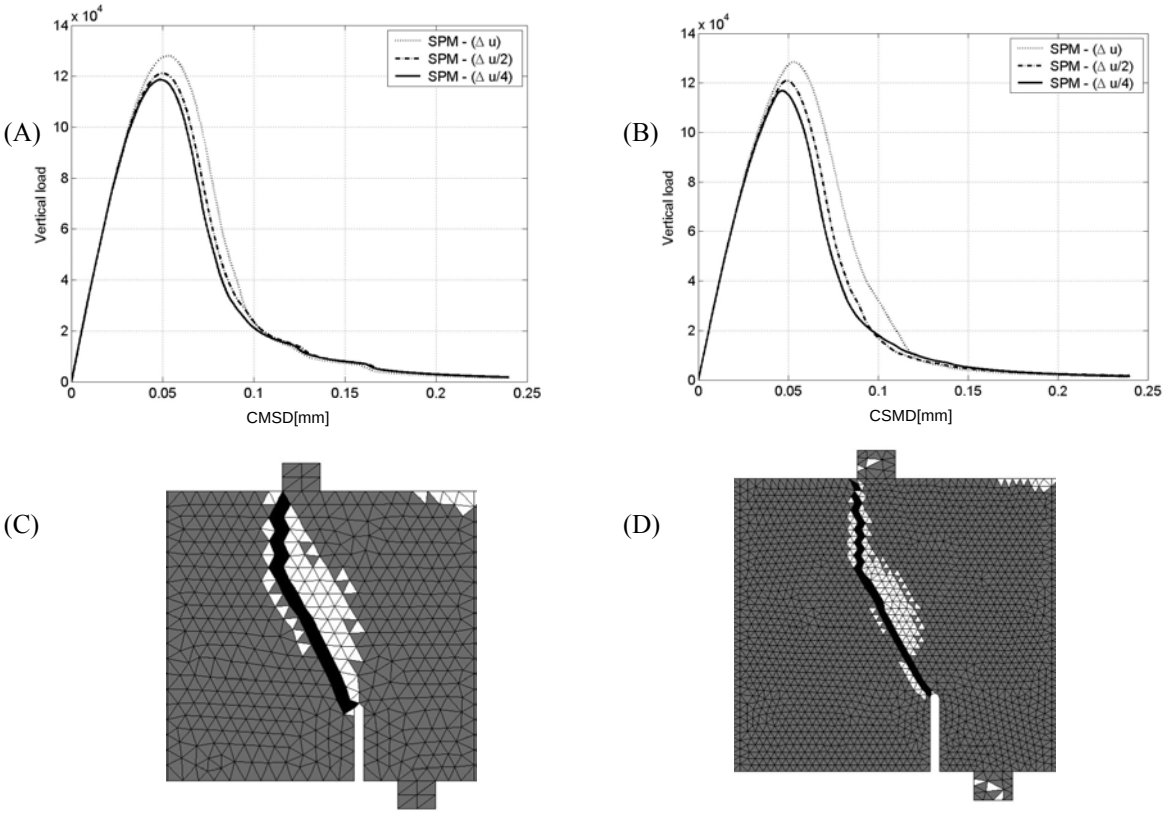


Figure 12: Four point beam bending test.
Load *vs.* CSMD curves for three different values of the control parameters: (a) mesh1, (b) mesh2.
Crack paths: (c) mesh1, (d) mesh2.

### 3.2 Numerical simulation of dynamic fracture problems

Two simulations are presented in this section. The first one, previously presented by Falk *et al.* in [4], is a square PMMA specimen displaying a high velocity crack propagation front. Differences with the numerical approach reported in [4] are presented. It is also pointed out the capability of the presented cohesive model to capture correctly the most important phenomenological aspects of dynamic fracture, that is, the crack tip velocity, the typical unstable crack branching phenomena and the morphology of the dynamic fracture of brittle materials. We adopt the work of Sharon *et al.* [13] in order to compare their experimental measures in PMMA specimens with our numerical results.

The second example is the well known Kalthoff's experimental test that has been numerically simulated and reported by Belytschko *et al.* in [6].

#### 3.2.1 Prediction of dynamic fracture in PMMA

We study the crack propagation problem in a square specimen with sides of 3.0 *mm* and a notch of 0.25 *mm* long (see Figure 13). The analysis is held in plane strain mode by imposing a vertical constant velocity of 3000 *m/seg* on the top and bottom edges.

The material corresponds to Polymethil-metacrilate (PMMA) which is characterized by an

ultimate stress $\sigma_u = E/25 = 129\,MPa$, a Young modulus $E = 3.24\,GPa$, a Poisson's ratio $\nu = 0.35$, a fracture energy $G_f = 0.352 N/m$ and a density $\rho = 1.19 g/cm^3$. These data have been taken from Falks *et al.* [4] and are slightly different from that presented in Sharon *et al.* [13]. With the presented values we can define the dilatational wave speed $c_d = \sqrt{\frac{\lambda + 2\mu}{\rho}} = 2090 m/seg$, the shear wave speed $c_s = \sqrt{\frac{\mu}{\rho}} = 1004 m/seg$ and the Rayleigh wave speed : $c_R = 938 m/seg$. Considering the characteristic dimension of the specimen and the former wave speeds, the loading condition imposed can be classified as a slow action.

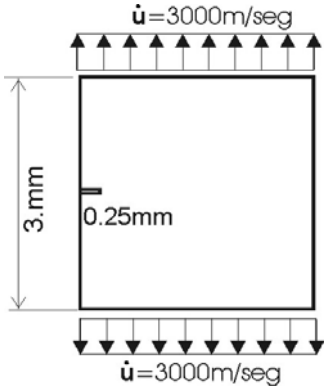


Figure 13: PMMA square block

Following to Falk *et al.* [4], we have modeled the problem using three uniform meshes (to avoid dispersion effects) of 80x80, 120x120 and 240x240 FE, here denoted Mesh 1, Mesh 2 and Mesh 3. The element sizes of these meshes are $50\mu m$, $25\mu m$ and $12.5\mu m$ respectively. Mesh 1 and 2 have a structured distribution of elements along the symmetry x-axis which is favorable to the propagation of a horizontal crack. On the other hand, Mesh 3 shows an arbitrary distribution of elements.

The cohesive zone size for this material is $l_{coh} = G_f E/\sigma_u^2 \approx 68\mu m$. Therefore, we are modeling the cohesive zone by means of 4 or 5 finite elements in the finest Mesh 3. Furthermore, considering a crack tip propagation velocity of 800 *m/seg*, the maximum we have obtained in the simulation, the crack tip is crossing a segment equivalent to the cohesive zone in time intervals of the order of $\Delta t \approx 68\mu m / 800 \cdot 10^6 (\mu m/seg) = 8.5 \cdot 10^{-8} seg$. In the present simulations we have used a Newmark integrator scheme with time steps ranging from $1.25 \cdot 10^{-9} seg$ to $0.5 \cdot 10^{-9} seg$. We have observed that the correct capturing of the branching phenomena was only possible to be reached by using this very small time step increment. It is not clear for us the reasons of this strong restriction. Probably it is due to the characteristic physical instability of the phenomenon that we are simulating. It should be noted that before the onset of crack branching, even after damage and crack propagation processes have started, the time steps could be chosen until two orders greater ($1 \cdot 10^{-7} seg$), maintaining the numerical stability of the scheme and without introducing an excessive integration error.

## Analysis of the results

### 1) Crack tip velocity

In Figure 14-a, it is depicted the crack tip position as a function of time. Figure 14-b plots the crack tip velocity, which have been evaluated as the numerical derivative of the curves in Figure 14-a. In this figure we also present the results reported by Falk *et al.* where two different implementation of a discrete cohesive model were used.

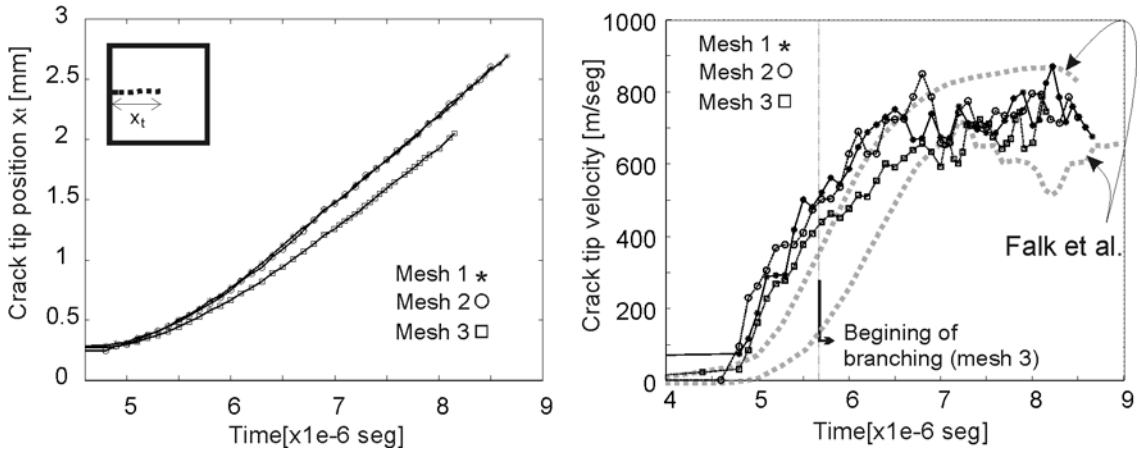


Figure 14. PMMA square block. crack propagation velocity

Even though the crack tip position of Mesh 3 is slightly different to that shown by meshes 1 and 2, which can be due to the above mentioned different mesh design along the x-axis, it can be observed that the maximum velocity are similar in all cases. Our results agree with that reported by Falk *et al.* [4] saving that we have obtained a higher initial acceleration with a final crack tip velocity slightly lower.

### 2) Crack pattern morphology

The presented numerical approach is able to capture the crack branching effect, typical of dynamic fracture problems, as is shown in Figure 15. It is displayed in Figure 15-a, b and c the distribution of cracks at the end of the simulation process for the three meshes. There, the black zone corresponds to active elements, or cracks in opening mode, while the gray zone represents elements that previously have been activated but that at the end of the simulation process are arrested. Figure 15-d, e and f show the iso-displacement curves representing the effect produced by the strain localization phenomenon.

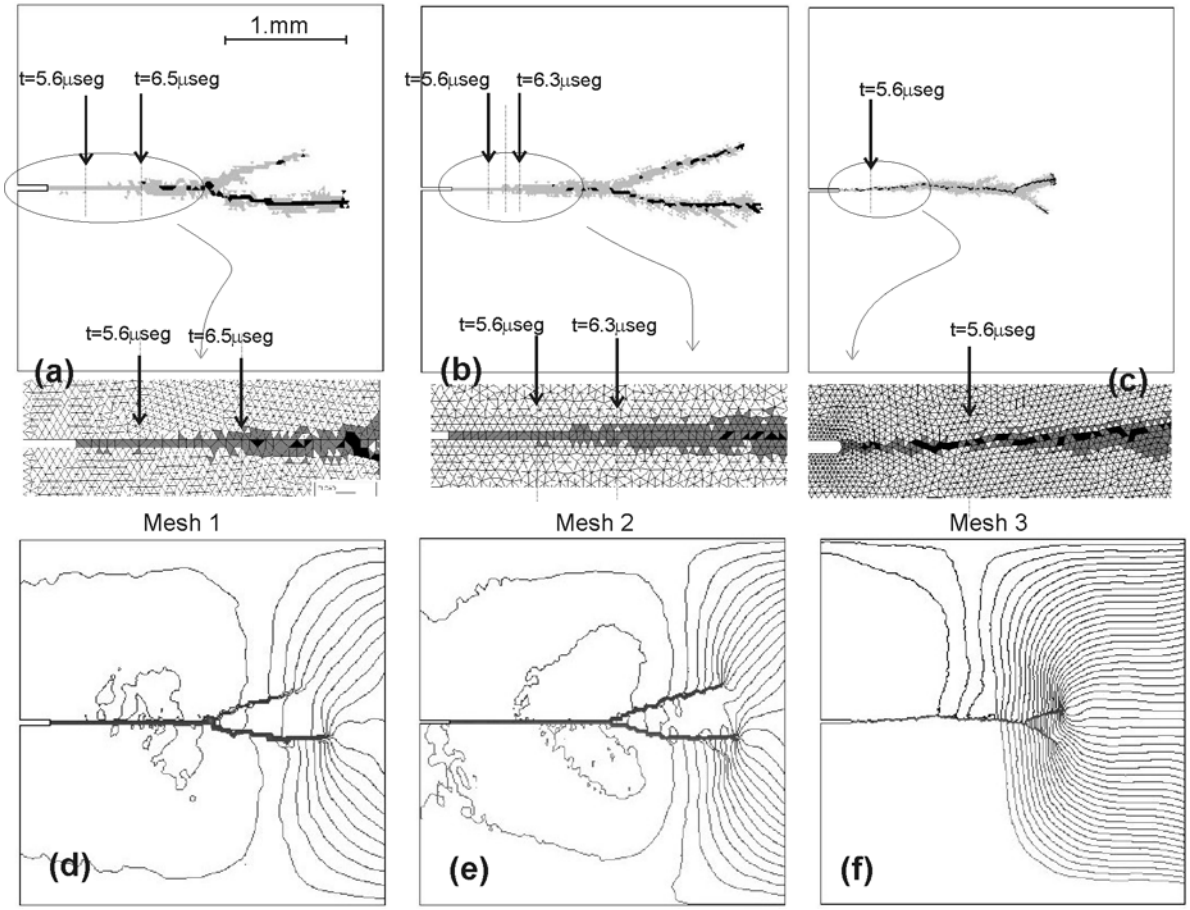


Figure 15. PMMA square block.
(a), (b), (c) Crack paths for Mesh 1, for Mesh2 and for Mesh3
(d), (e), (f) Curves of iso-displacement for Mesh 1, for Mesh2 and for Mesh3
(Results of Mesh1 and Mesh2 are at time $t = 8.7\mu seg$ meanwhile results of Mesh3 are at time $t = 8.1\mu seg$ )

The crack distribution morphology of the numerical simulation follows rather closely the experimental observation reported by Sharon *et al.* in [13]. This experiment was done using the same material PMMA, but with different boundary conditions and specimen dimensions. However these differences, it would be expected a similar crack distribution pattern produced by the unstable fracture propagation phenomena there reported.

In fact, analyzing the results presented in Figure 15c and f, we can observe an initial although not well defined branching in Mesh 3, between the times $5.6 - 5.8\mu seg$ (see also the zoom in Figure 16). This instant corresponds with a crack tip velocity of the order of $v_c \sim 400 m/seg \cong 0.43 c_R$. In the experimental test of Sharon *et al.* it is reported a velocity level, $v_c \cong 0.34 c_R$, as the critical one producing branching. In the finest mesh, a perceptible branch does not appear until to reach the time $6.4\mu seg$. In the coarse mesh, the widening of the activated element zone is observed in a later time.

Therefore, we can conclude that the simulation captures the observed behavior described by Sharon *et al.* For velocities $v < v_c$, a single straight crack is obtained. When the velocity increases and $v \cong v_c$, small lateral branches appear, corresponding with our widening of the element active band. Finally, when $v > v_c$, finite length branches are observed in the numerical simulation agreeing with the experimental observations.

Figure 16 is a close-up of the crack process carried out with the finest mesh. Another ex-

perimental issue is observed to be correctly captured by the model. The angle which the crack branches form with the principal one is between $24^o - 32^o$. The experimental observations show that this angle is between $27.3^o - 31^o$ reported in Sharon *et al.* [13] and additional references cited therein.

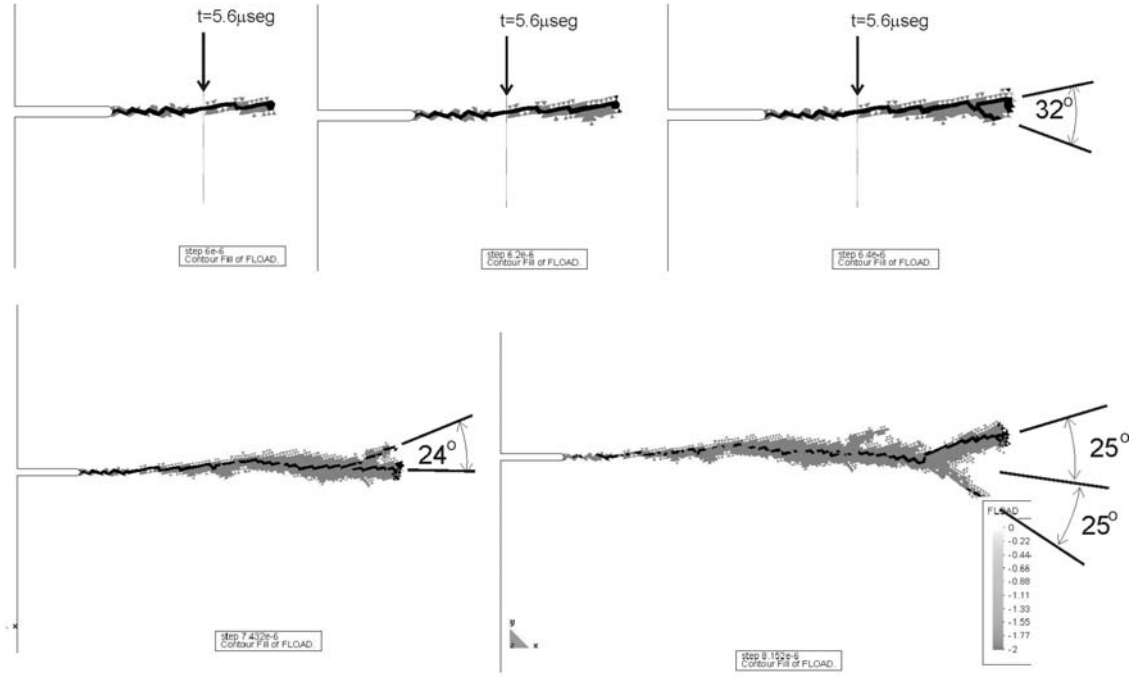


Figure 16. PMMA square block. crack propagation pattern, Mesh3, times: 6.0, 6.2 and 6.4, 7.4 and 8.1, showing the angles of the crack branches.

Another morphologic characteristic of this phenomenon is the length of the crack branches. In the mentioned experimental work, the authors conclude that the length of branched cracks, in the plane x-y when the main crack propagates along the x-axis and being y the distance from the main crack, follows a potential law: $y = 0.2x^{0.7}$ (dimensions in mm). This law is plotted in Figure 17. Again, it can be observed that the simulation agrees reasonably well with this experimental fact.

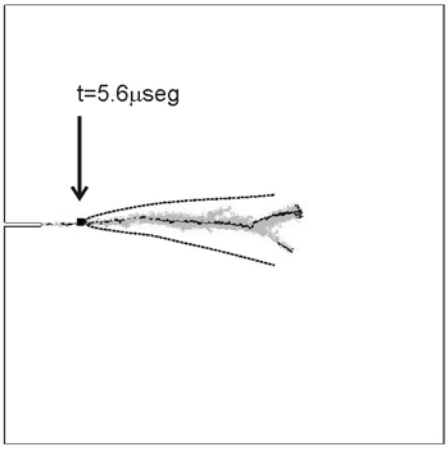


Figure 17. PMMA square block. crack propagation pattern, mesh3.

Comparison of the mean branch profile with the power law of Sharon *et al.* [13]

Figure 18 show a sequence, along time, of the principal stress field determined with the finest mesh. It can be observed a dispersed stress wave starting at approximately the onset time of crack branching and centered in that point.

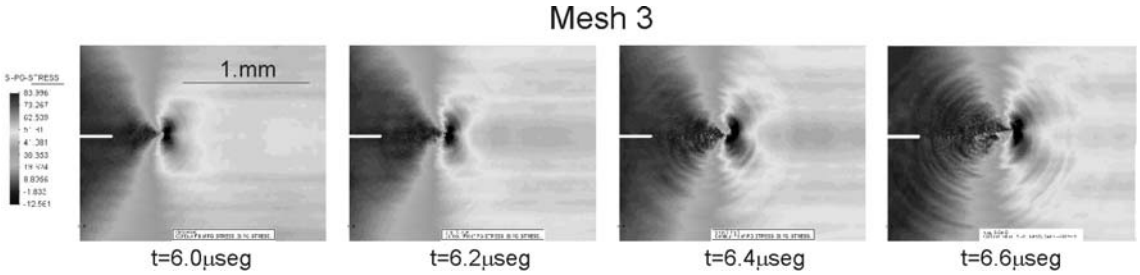


Figure 18. PMMA square block. maximum principal stress $\sigma_1$ obtained with the mesh 3 at different times.

### 3) Energy dissipation

Figure 19 show, for the three meshes, the dissipated energy $D$ along the process. This energy, is given by the external loads energy $P_{ext}$ minus the deformation energy $W$ and the kinetic energy $K$:

$$D = P_{ex} - W - K \,. \tag{24}$$

These terms are evaluated as follows:

$$\begin{aligned} P_{ex} &= \sum_{i=1}^{nstep} F^{ext}_{n+1/2} \cdot \Delta \mathbf{u}_{\Gamma} \quad ; \quad \text{in the Newmann contour} \\ \mathrm{W} &= \sum_{i=1}^{nstep} \sigma^{t}_{n+1/2} \cdot \Delta(\bar{\boldsymbol{\varepsilon}} - (\mathbf{b}^{+} \otimes \boldsymbol{\beta})^{s}) d\Omega; \\ K &= \frac{1}{2} \mathbf{v}_{n+1} \cdot \mathbf{M} \cdot \mathbf{v}_{n+1} \end{aligned} \quad . \tag{25}$$

From Figure 19 it can be observed a slight difference of the finest mesh response arising after the crack branch phenomenon starts.

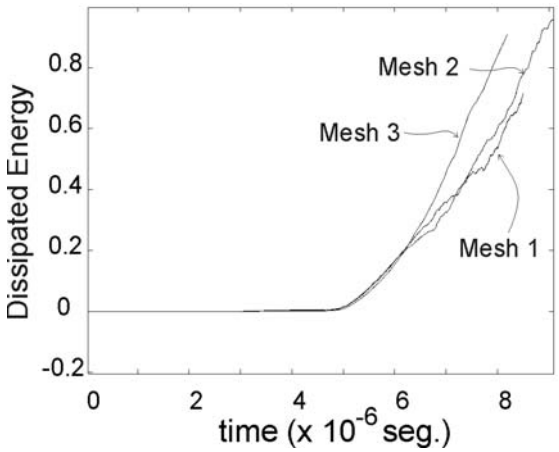


Figure 19. Square block of PMMA. Dissipated energy along the process.

### 3.2.2 Numerical simulation of the Kalthoff's experiment

The experimental test reported by Kalthoff consists of an edged-cracked plate that is impacted by a projectile, as is shown in Figure 20. He observed that modifying the projectile impact velocity, either a ductile or a fragile mode of fracture is developed in the specimen. At lower impact velocities, a mode I crack opening is observed. The cracks propagate from the notch root towards to the specimen top and bottom forming an angle of $\approx 70^o$ with the horizontal line. Following the work of Belytschko *et. al* [6], we simulate this mode of fracture by adopting the model described in that work. The plate is supposed to deform under plane strain conditions. The projectile impact is modeled imposing a velocity on the contour $\Gamma$ of value $\mathbf{v}_o = 16.5 m/seg$ and the material parameters are: $E = 190.GPa$, $\nu = 0.3$, $\sigma_u = 844MPa$, $G_f = 22170.N/m$ and $\rho = 8000 kg/m^3$. The Rayleigh wave speed results: $c_R = 2799.m/seg$. We solve the problem using a mesh of 14316 FE, with elements of sizes $1.25mm$ (the characteristic length of the material is $l_{ch} = EG_f/\sigma_u^2 \approx 6.mm$). The time integration step is $\Delta t = 1 \cdot 10^{-8} seg$.

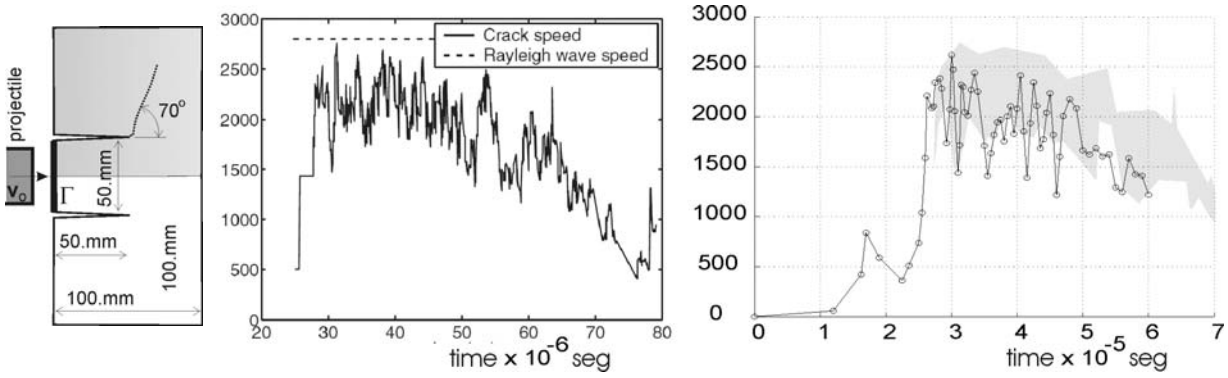


Figure 20: Kalthoff's experiment. Crack tip velocity; a) experimental model, b) experimental results taken from Belytschko *et al.*; c) present numerical results

Figure 20-b shows the experimental crack tip velocity and Figure 20-c the same value that has been numerically obtained with the present simulation. Superposed on the same figure, the gray zone corresponds to the experimental results of Figure 20-b. The fitting between both results is reasonable good.

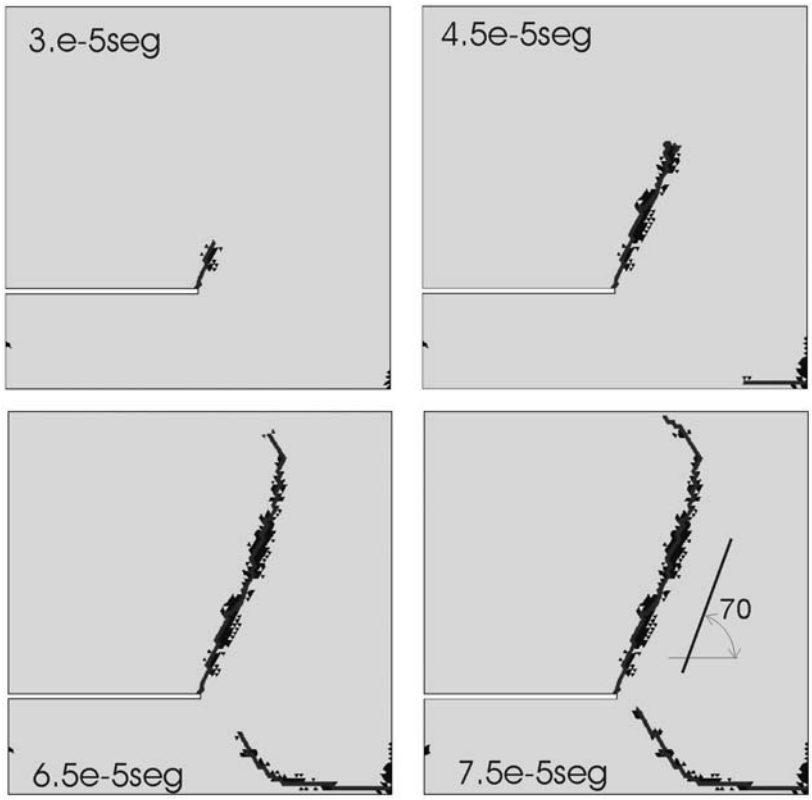


Figure 21: Crack tip evolution in the Kalthoff's experiment; snapshots at different times.

Figure 21 displays the crack advance along the time. In this case, the simulated crack pattern agrees with the experimental observation.

## 4 CONCLUDING REMARKS

Some aspects of the phenomenology related with crack dynamics problems, such as crack tip velocity, morphology of the crack distribution in the specimen, etc., can be acceptably captured by the model here presented. Although it was known from previous works that cohesive models have this property, the present approach has the following additional benefits:

- If compared with the interface models, the present embedded strong discontinuity approach is more flexible to represent the discontinuity path across the mesh.
- It does not require an algorithm to predict the discontinuity path across the mesh.
- It does not require a specific treatment in those elements that are intersected by the crack branching.

**Acknowledgements**

The first, third and fifth authors acknowledge the support of CONICET- Argentina. Financial support from the Spanish Ministry of Science and Technology of Spain, through grants BIA2005-09250-C03-03, is gratefully acknowledged.

## REFERENCES

[1] E. Sharon, S.P. Gross, J. Fineberg: "Local crack branching as a mechanism for instability in dynamic fracture", Physical Rev. Letter, 1995, vol. 74, No. 25, pp.5096-5600.

[2] P. Klein, H. Gao, "Study of crack dynamics using the virtual internal bond method", in: Multiscale deformation and fracture in materials and structures, James R. Rice's 60th Anniversary Volume, Kluwer Academic Publishers, Dordrecht, The Netherlands, 2000, pp. 275–309.

[3] Xu, Needlemann: "Numerical simulation of fast crack growth in brittle solids", J. Mech. Physics of Solids, 1994, vol.42, pp.1397-1434.

[4] M.L. Falk, A. Needlemann, J.R. Rice: "A critical evaluation of dynamic fracture simulation using cohesive surfaces", J. de Physique IV, Proc. 2001, pp. Pr-5-43 to Pr-5-50.

[5] A. Pandolfi, P.R. Guduru, M. Ortiz: "Three-dimensional cohesive elementsof dynamic fracture in C300 steel", Int. J. Solid. & Struct. , 2000, vol.37, pp. 3733-3760.

[6] T. Belytschko, H. Chen, J. Xu, G. Zi: "Dynamic crack propagation based on loss of hyperbolicity and a new discontinuous enrichment", Int. J. Num. Meth. Eng., 2003, vol.58, pp.1873-1905.

[7] J.C. Simo J.,Oliver J. "A new approach to the analysis and simulation of strong discontinuities". presented at Fracture and Damage in Quasi-brittle Structures, 1994.

[8] J.C. Simo, J.,Oliver, J.,Armero F. "An analysis of strong discontinuities induced by strain-softening in rate-independent inelastic solids". Computational Mechanics, vol. 12, 277-296, 1993.

[9] J.M. Sancho, J. Planas, D.A. Cendón, E. Reyes and J.C. Gálvez: "An embedded crack model for finite element analysis of concrete fracture", Engineering Fracture Mechanics, In Press, Corrected Proof, Available online 6 March 2006,

[10] Oliver J.,Huespe A.E.,Blanco S.,Linero D.L. Stability and robustness issues in numerical modeling of material failure in the strong discontinuity approach. Comput. Methods Appl. Mech. Engng. (accepted for publication), 2005.

[11] Rots J.G., Computational Modeling of Concrete Fractures. PhD Thesis, Delft University of Technology, 1988.

[12] Oliver J.,Huespe A.E.,Pulido M.D.G.,Chaves E. From continuum mechanics to fracture mechanics: the strong discontinuity approach. Engineering Fracture Mechanics, 2002, vol. 69, pp. 113-136.

[13] E. Sharon, J. Fineber, "Microbranching instability and the dynamic fracture of brittle materials", Physical Rev. B, 1996, vol. 54, No. 10, pp.7128-7136.